Magnetohydrodynamic levitation for high-performance flexible pumps

Yoav Matia[a,b,1] [ID], Hyeon Seok An[a,1], Robert F. Shepherd[a,2] [ID], and Nathan Lazarus[c,2]

We use magnetohydrodynamic levitation as a means to create a soft, elastomeric, solenoid-driven pump (ESP). We present a theoretical framework and fabrication of a pump designed to address the unique challenges of soft robotics, maintaining pumping performance under deformation. Using a permanent magnet as a piston and ferrofluid as a liquid seal, we model and construct a deformable displacement pump. The magnet is driven back and forth along the length of a flexible core tube by a series of solenoids made of thin conductive wire. The magnet piston is kept concentric within the tube by Maxwell stresses within the ferrofluid and magnetohydrodynamic levitation, as viscous lift pressure is created due to its forward velocity. The centering of the magnet reduces shear stresses during pumping and improves efficiency. We provide a predictive model and capture the transient nonlinear dynamics of the magnet during operation, leading to a parametric performance curve characterizing the ESP, enabling goal-driven design. In our experimental validation, we report a shut-off pressure of 2 to 8 kPa and run-out flow rate of 50 to 320 mL·min^{-1}, while subject to deformation of its own length scale, drawing a total of 0.17 W. This performance leads to the highest reported duty point (i.e., pressure and flow rate provided under load) for a pump that operates under deformation of its own length scale. We then integrate the pump into an elastomeric chassis and squeeze it through a tortuous pathway while providing continuous fluid pressure and flow rate; the vehicle then emerges at the other end and propels itself swimming.

magnetohydrodynamic levitation | soft displacement pump | fluid–structure interaction | viscous flow | soft robotics

1. Introduction

A large number of soft robots use fluidic elastomer actuators (FEAs) powered by pumps (e.g., refs. 1–17). These pumps, the hearts of soft robots, are typically electrically powereddisplacement pumps due to their availability, efficiency, performance curves, and control simplicity. An example of a typical electrically powered displacement pump is the BTC IIS (Parker-Hannifin), which is rigid and bulky. When used, these types of pumps necessitate centralizing them, routing the pressurized fluid via long channel lengths to the actuator locations, and use valving to control when they are pressurized, as evident in characteristic works, such as Tolley et al. (10) and Aubin et al. (18).

The use of pumps with mechanical properties more similar to FEAs would allow for the decentralization and distribution of displacement pumps across the volume of soft robots. The benefits of this approach would be numerous: 1) The number of pumps in one machine could be increased for faster and more forceful robots; 2) they could be placed in closer proximity to actuators for improved efficiency; 3) the number of valves could potentially be reduced for smaller form factors; and 4) most importantly, the beneficial compliance of soft robots would be maintained.

In this regard, there are several promising and elegant examples of pumps made entirely of compliant materials for use in soft robots, such as those of Cacciucolo et al. (19) and Diteesawat et al. (20). Other examples (13, 21–28) offer the potential for efficient, distributed fluidic actuation or analogous approaches to soft displacement and rotary pumps (13, 29–42), and, while they all incorporate soft materials or could be envisioned as a viable pumping solution for soft robotic application; none report performance under deformation, limiting their practical application. Thus, there still remains an important need for a compliant displacement pump that offers high flow rates, $q = O(10^2)$ mL·min^{-1}, and pressures, $p = O(10^5)$ Pa, at a system duty point (i.e., system and pump-curve intersection) compatible with human-scale FEA systems, $O(10^{-1}$ to $10^0)$ m. Further, scalable and continuous performance under quasistatic or

Significance

This paper explores a scalable approach to making soft robotic hearts and presents an elastomeric pump uniquely suited for soft robotics challenges. We leverage the underlying principle of magnetohydrodynamic levitation to create a soft, elastomeric, solenoid-driven pump. The pump provides a duty point (i.e., the pressure and flow rate provided under load) 2-orders-of-magnitude greater than any reported to date for pumps that operate under deformations of their own length scale. We elucidate avenues for tailoring performance in goal-oriented design by providing both scaling laws and explicit analytic results, validated by experimental demonstrations. This work constitutes a first step in developing a practical deformable pump that will serve as a foundation for future advances in untethered soft pump technology.

dynamic deformation should also be a feature of this pump to facilitate technology transfer.

The major challenge facing the development of a deformable displacement pump is the need to maintain a seal under deformation. This means maintaining a separation between the high and low potential fluid while providing a physical gap, on the order of the local curvature, between adjacent interacting components (e.g., an impeller or piston, or equivalent within the housing, to avoid mechanical jamming). In our work, we use ferrofluids to manage this gap. Therefore, of special relevance to this work is research regarding ferrofluids' use as the medium in making a fluidic seal in either journal bearings (43–47) or other rigid applications; for example, refs. 48–53, to name just a few. In addition, examination of rigid ferrofluid-based pumps, such as refs. 54–59, exemplifies the inherent limitations in extending the notion of a fluidic seal to the displacing component being made entirely of liquid— i.e., making a liquid piston or vane—whereby relying on cohesion forces (i.e., surface tension) to generate appreciable pressure gradients $\Delta p = O(10^0)$ kPa, and, as these are inversely related to gap width, we have to operate in gap regimes that are too narrow for utility, resulting in very low flow rates less than $q = O(10^{-1})$ mL·min^{-1}.

This paper explores an approach to making soft robotic hearts, whereby the traditional concept of ferrofluid gap management is extended to loosely fitted magnetic cores that act as pistons and are centered by leveraging magnetohydrodynamic lubrication. The ferrofluid coating centers the core as it moves along the flexible tube and forms a seal, bridging over a specified physical gap of $C = 0.25$ mm, selected as such to allow the magnetic core in our system to travel without jamming as the pump takes on a radius of curvature of its own length scale, $R_c \leq 100$ mm. Further, we provide the scaling laws for the magnetohydrodynamic lubrication mechanism in such systems with respect to pressure, flow rate, size, and radius of curvature, thus proposing a scalable principle mechanism for future advances in soft-pump technology.

While the field of hydrodynamic lubrication has been studied extensively over the years, with or without magnetic force involvement, the nonlinear nature of the physics governing such systems caused prior efforts to avoid explicit dynamic solutions of the lubrication-layer thickness evolution over time. Therefore, these efforts usually set the lubrication layer as constant (60, 61), or consider time not as an independent variable, but, rather, as an input parameter, setting eccentricity and rate of change as constant (62, 63), resulting in a static problem governed by an elliptical equation. Others use planar configurations (61, 64), focus on experimental and numerical examination (61, 64, 65), or a combination of the above.

In this paper, we present an approximate explicit solution of the predictive model for our soft robotic heart that uses perturbation theory to capture the nonlinear dynamics of magnetohydrodynamic lubrication in a nonplanar configuration. We then experimentally demonstrate that this elastomeric solenoid-driven pump (ESP) can maintain continuous performance under large deformation—i.e., up to 30% in axial strain and a radius of curvature of its own length scale—as well as supply the design rules to correlate physical parameters to the desired deformation (for main text nomenclature, see *SI Appendix*, section A.1, Table S1).

In Fig. 1, we provide a visualization of novelty; we show the proposed ESP operating at the largest duty point yet reported for pumps that continue to operate while deformed (for literature comparison details, see *SI Appendix, section A.2, Table S2*). Last, we provide the insight and scaling laws required to produce
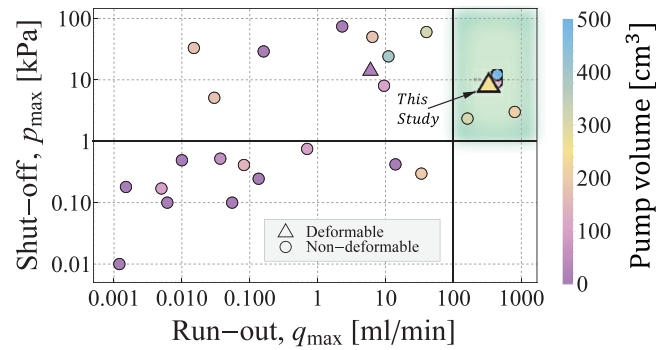

Fig. 1. Shut-off (max pressure, no flow) vs. run-out (max flow, no back-pressure) performance of comparable state-of-the-art systems. Visualization of novelty, largest work-point reported to date for pumps that operate under large deformations (of its own length scale). All other pump technologies in its performance order-of-magnitude are nondeformable pumps.

a goal-driven design of this pump system, tailored to soft robotics' unique challenges.

2. Materials and Methods

Fig. 2 presents the studied configuration of an elastically compliant soft robot heart, the ESP. In Fig. 2A, we show a three-dimensional (3D) section cut and present our system's fundamental physical quantities at work. By applying current to the solenoid coil, we generate a magnetic field $\vec{B}_{coil}$, attracting a rigid permanent magnetic core of field $\vec{B}_m$, and driving it at velocity $\vec{u}_{mag}$ via the dipole–dipole interaction. This core (interchangeably denoted the "magnetic piston core") is sheathed with a layer of ferrofluid (FerroTec EFH1), in which hydrodynamic lubrication generates viscous pressure p by the forward motion, centering the core and preventing contact with the walls, addressed in detail in Section 4.1.

Fig. 2B presents the experimental workbench setup used to measure the pump-performance curve outside a robotic system. We show the ESP connected to fluid reservoirs: one at the inlet and one at the outlet. The outlet tubing is fitted with a flowmeter (Renesas, catalog no. FS2012-1020-NG), a pressure sensor (Honeywell, catalog no. SSCDANN030PAAA5), and a Precision Flow-Adjustment Valve (McMaster-Carr) providing back-pressure load. Workbench peripheral components standing in for the robotic system include: a microcontroller unit (MCU) (Arduino Uno) and Keithley 2400 direct-current power supply, providing the required 0.17 W (1 V and 0.17 A). Pump-assembly dimensions are (width × length × height) = (40 × 71 × 8) mm, and it is made of silicone urethane elastomer SIL 30 (CARBON, Inc.) with an elastic modulus of $E = 1.8$ MPa. Fig. 2 B, *Inset* illustrates the pump's internal structure, featuring seven solenoids of wire density $M[winding$ m$^{-1}] = 5,760$ threaded over the core tube, magnet end stoppers, inlet and outlet joints, and four unidirectional flow valves. For more details, see *SI Appendix, section A.3*.

In Fig. 2 C–E, we illustrate the role of the four integrated flow valves, creating unidirectional flow from inlet to outlet as the magnetic core piston is cycled back and forth along the core tube. Red cross-marks denote which valves are at closed state, and red and blue fluid lines indicate high and low pressure, respectively.

Particular attention is given to the dimensioning of rigid components within our system, i.e., ball bearings, solenoid coils, and the magnetic piston core. The ball bearings (used for the unidirectional valves) add no constraint on the system's elastic compliance, being in a loose fit of their own length scale ($d_{ball} \approx 3.5$ mm). Conversely, the pump's ability to maintain continuous performance under elastic deformation is restricted by the solid magnet piston core and the number of solenoids, limiting bending deformation, as would a vertebra. First, we set the pump's operational envelope and require continuous operation under deformation of its own length scale; we thus set the limit for the radius of curvature to be $R_c \approx 100$ mm; see illustration in Fig. 2F. We then select the magnetic piston core to match the overall scale of the pump assembly, namely, a commercially available N52 Neodymium magnet with a diameter of $d_m = 2r_m = 4$ mm and a length $l = 6.315$ mm, in accordance with which we determine the length of the solenoid coils $l_c = l$. Having established the piston-core dimensions and curvature limits, we can then determine the gap required, $C = 0.25$ mm, and,
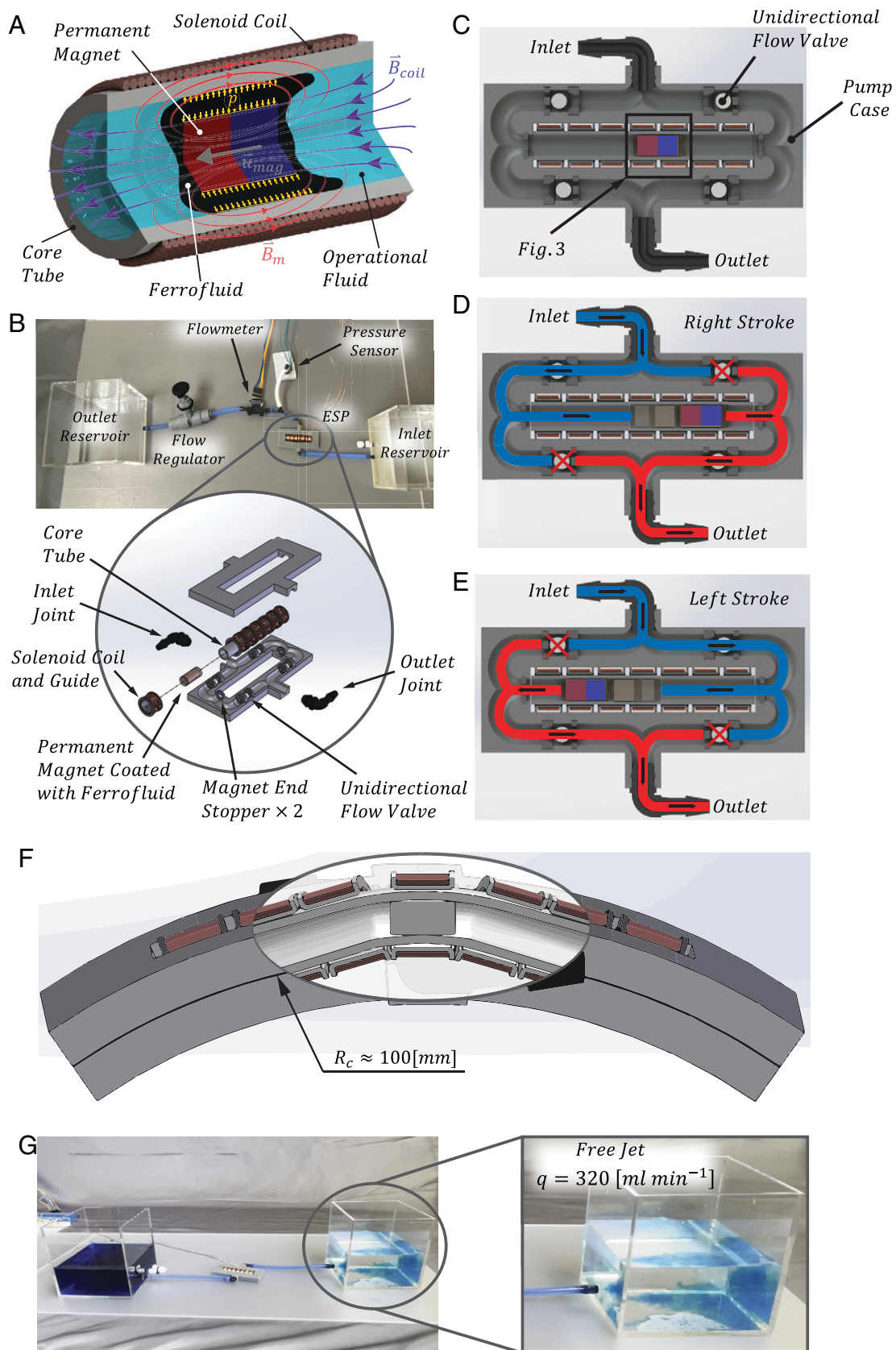
Fig. 2. Illustration of the ESP configuration used in both modeling and experiments. (*A*) A 3D model with key components and physical quantities. (*B*) Workbench setup used in the acquisition of experimental data. *B*, *Inset* illustrates an exploded view of the internal structure of an ESP with key top-level components. (*C*) Cross-section view of ESP; the black frame indicates the focus of Fig. 3. (*D* and *E*) Cross-section view of ESP in operation. Snapshots of magnetic core right and left heading strokes with an indication for the state of the one-directional valves; red and blue fluid lines indicate high and low pressure, respectively. (*F*) Illustrative image of our designed ESP under deformation (bending) showing the loosely fitted magnetic core jamming upon exceeding the design-intended limit for the radius of curvature $R_c \approx 100$ mm, thus emphasizing the particular importance of a goal-driven design for rigid components in our system. (*G*) Visualization of pump potency, generating a free jet, with flow rate measured at $q \approx 320$ mL·min^{-1}.

respectively, the diameter of the enveloping tube inner wall $d_w = 2r_w = 4.5$ mm. For a detailed discussion on bending strain relation to geometric parameters, see Section 5 and *SI Appendix*, section A.4.

3. Experiment Procedure

Using our benchmark setup (Fig. 2*B*), we characterize pump performance at both the deformed and free states. We start the system from rest with the flow regulator fully closed and initiate the MCU supplying 1V and 0.17 A to the solenoid train. We then set the nominal solenoid relay period to $\tau_r \approx 0.019$ s, i.e., the activation period of a solenoid in a sequence. Based on the viscous-elastic characteristic time scale $t^* \sim \pi l \mu / \varepsilon^2 \kappa_f$ (see derivation in Section 4.1), we calculate the system achieving steady state after a time scale of the order $t^* \approx 0.113$ s. To ensure that we have achieved steady state prior to collecting data, we allow the system 1 min to stabilize. We then take pressure-sensor readings, evaluate flow rate using both a flow-meter and by collecting the outlet spillage for 2 min in a 1,000-mL glass beaker, and normalize for water density at room temperature. Repeating this process for 20 measuring points, differentiated by incrementally increasing flow rate using the flow regulator, we generate the pump-performance curve. Experimental data for all plots in this work represent one-sigma certainty acquired over seven experiments per pump and five separate pumps tested.

Fig. 2*G* offers a visual indication of the pump's potency, generating a free jet with a flow rate measured at $q = 320$ mL·min^{-1}. We report continuous performance in the order of $p = O(1)$ kPa and $q = O(10^2)$ mL·min^{-1} over a range of elastic deformation up to a radius of curvature of the pump's length scale. For a detailed discussion of scaling laws for geometry, deformation, and performance, please refer to Sections 4 and 5.

4. Analysis

Providing the theoretical framework for our experimental system, we present two separate models for two separate governing mechanisms in the system. Together, these provide insight and predict the system's dynamic behavior. The first is the single-phase lubrication layer: We calculate the friction and pressure inside the fluid-seal domain using lubrication theory. Integrating with the force-balance equations, we correlate back-pressure Δp, downstream effective flow velocity u_m, and electromagnetic actuating force f_b (Eq. **1.11**). The model assumes $u_m = u_{mag}$, where u_{mag} is the effective average velocity of the magnet during operation. Furthermore, it is assumed that the product of u_m and core tube-inner cross-section gives us the pumped flow rate q mL·min^{-1} vs. pressure Δp kPa—predicting the nonlinear inverse relation of the pump's performance curve.

The second provides the mechanism correlating the above-mentioned prediction with our experiments, where the actual magnet velocity $u_{mag} = z_0/\tau_r$ is held constant, fixing the solenoid relay time actuation τ_r. We are then left to reason the means by which a constant velocity-driven positive displacement pump provides a varying flow rate. We utilize the equation-based modeling capabilities of COMSOL Multiphysics 5.5 (*SI Appendix*, section A.7) and show the emergence of Taylor–Saffman instability—i.e., viscous fingers—with a unique stable developed pattern emerging in the presence of the system's restoring magnetic force. We thus show how an effective flow-rate "leak" dependent on back-pressure Δp is maintained past the liquid seal to enforce mass conservation.

4.1. Lubrication Theory Modeling, Prediction of the Nonlinear Inverse Relation of Pressure to Flow Rate.
We begin by formulating the predictive model characterizing the steady state and dynamic performance of an ESP. It consists of a cylindrical core tube, inside of which is a levitated magnetic core coated with ferrofluid. This coating provides a seal capable of maintaining its integrity as the pump deforms during operation and the viscous pressures required for magnetohydrodynamic levitation to prevent the solid–fluid piston from jamming during operation. Fig. 3*A* illustrates the axial cross-section of the proposed system. Fig. 3 *B* and *C* illustrates the magnet axial degrees of freedom; the solenoid wire is omitted for visual clarity.

In order to gain insight into the performance of an ESP system and the results presented here, we aim to model both the magnet dynamics during a stroke in the reciprocating cycle (Fig. 4 *A* and *B*) and the performance curve describing the pump performance fully (Fig. 4*C*). Based on the effective downstream fluid velocity u_m set to be the average magnet forward velocity u_{mag}, and knowing core tube-inner cross-section, we can calculate the pumped flow rate q mL·min^{-1} vs. pressure Δp kPa.

We define vector variables using bold letters, direction vectors by hat notation, nondimensional variables by capital letters, characteristic values by an asterisk, and respective mth order-of-magnitude by a superscript (n). We define the small parameter $\varepsilon = C/l$, where C and l are the magnet–wall gap at the concentric position and the magnet length, respectively. We limit axial eccentricity by the ferrofluid gap $\lambda(t) \leq C$, as well as angular misalignment $\left(\alpha(t)l\right)/2 \leq C$; we set tube radial and axial deformation due to fluid pressure to be negligible, and, finally, both tube and magnetic core do not rotate about their axis. We consider the one-phase flow of ferrofluid seal in the narrow gap between the magnetic piston and the bounding tube wall as the magnet is driven forward. We assume the ferrofluid to be Newtonian and incompressible, and, by way of lubrication approximation (63), we formulate our governing equations for mass $\nabla \cdot \boldsymbol{u} = 0$, and momentum conservation, in terms of the Stokes equation $\nabla p = \mu \nabla^2 \boldsymbol{u}$. We define a moving, gap curvilinear cylindrical frame $(\hat{\tilde{\boldsymbol{r}}}, \hat{\boldsymbol{\theta}}, \hat{\boldsymbol{z}})$ centered at the magnet center of mass, where we define the curvilinear gap coordinate $\tilde{r}$ to range from $\tilde{r} = 0$ at the magnetic core surface (respective to cylindrical r_m in Fig. 3*A*) to $\tilde{r} = h$ at the enveloping tube inner wall (respective cylindrical r_w in Fig. 3*A*). We then set our system's boundary and initial conditions: The magnetic core translates axially $u_r(\tilde{r} = 0, \theta, z, t) = -\frac{\partial h}{\partial t}$, but does not rotate $u_\theta(\tilde{r} = 0, \theta, z, t) = \bar{\omega} = 0$, as the magnet is driven forward at $u_z(\tilde{r} = 0, \theta, z, t) = u_m$; the enveloping tube (i.e., core tube) is at rest $u_r(\tilde{r} = h, \theta, z, t) = 0$, $u_\theta(\tilde{r} = h, \theta, z, t) = 0$, $u_z(\tilde{r} = h, \theta, z, t) = 0$, and the entire system starts from rest $u_r(\tilde{r}, \theta, z, t = 0) = 0$, $u_\theta(\tilde{r}, \theta, z, t = 0) = 0$, $u_z(\tilde{r}, \theta, z, t = 0) = 0$. Last, we limit for small tilt angles $\alpha(t) \ll 1$ as $C \ll l$ and solve to obtain in dimensional form a special case of the Reynolds equation,

$$-\frac{\partial h^{(0)}}{\partial t} = -\frac{1}{12\mu}\frac{\partial}{\partial z}\left(\frac{\partial p^{(0)}}{\partial z}\left(h^{(0)}\right)^3\right) + \frac{u_m}{2}\frac{\partial h^{(0)}}{\partial z}, \qquad \textbf{[1.1]}$$

relating the ferrofluid viscous pressure field $p^{(0)}(\theta, z, t)$ with magnet radial position via gap height $h^{(0)}(\theta, z, t)$. Solving for viscous pressure $p^{(0)}$ with $p^{(0)}(\theta, z = l/2, t) = \Delta p_{pump}$ and $p^{(0)}(\theta, z = -l/2, t) = 0$, we then provide an explicit form for pressure and axial velocity profiles as dependent on the movement of the magnet inside the encapsulating core tube,
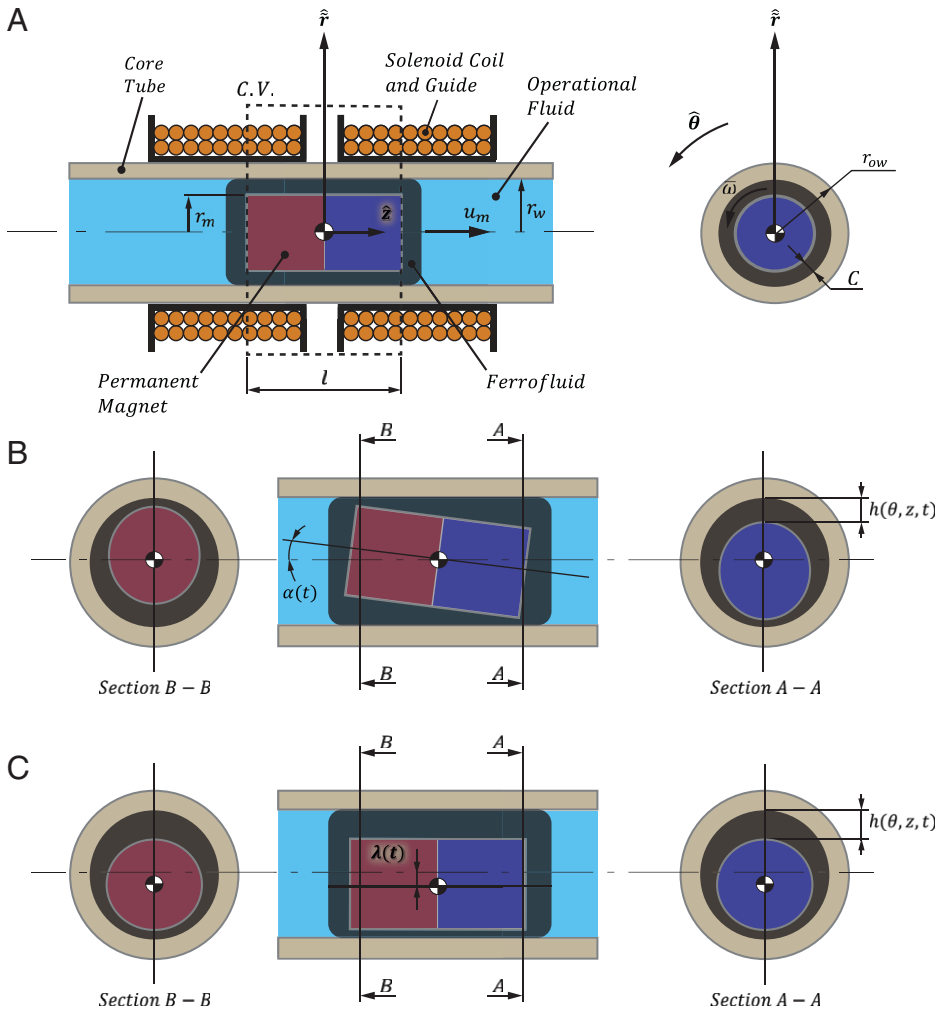
Fig. 3. System geometry, including section views for visual clarity. (*A*) System axial cross-section with the magnetic core axially centered (Control Volume denoted by C.V.). (*B*) Illustrating angular deviation of the magnetic core from a coaxial position. (*C*) Illustration of respective parallel deviation. For plates B and C, the solenoid coil surrounding the core tube was omitted for visual clarity.

$$p^{(0)}(\theta, z, t) = \frac{12\cos\theta}{\left(1 + \lambda(t)\cos\theta\right)^3} \frac{\partial\lambda(t)}{\partial t} \frac{\mu}{\varepsilon^2}\left(\frac{z^2}{2l^2} - \frac{1}{8}\right)$$

$$+ \Delta p_{pump}\left(\frac{z}{l} + \frac{1}{2}\right), \qquad \textbf{[1.2]}$$

$$u_z^{(0)}(\tilde{r}, \theta, z, t) = \frac{1}{2}\left(\frac{12\cos\theta}{\left(1 + \lambda(t)\cos\theta\right)^3} \frac{\partial\lambda(t)}{\partial t}z + \frac{l\varepsilon^2}{\mu}\Delta p_{pump}\right)$$

$$\left(\frac{\tilde{r}^2 - h\tilde{r}}{l^2\varepsilon^2}\right) - u_m\left(\frac{\tilde{r}}{h} - 1\right),$$

$$\textbf{[1.3]}$$

and the characteristic scale for pressure $p^* \sim \mu u_m/l\varepsilon^2$ and kinematics of the ferrofluid field $\varepsilon \sim C/l \sim C/r_m \sim u_r^*/u_m$. The observed pressure scaling implies very large pressures of the order $O(1/\varepsilon^2)$ generated by any deviation from the concentric position of the magnet λ and its temporal transients $\partial\lambda/\partial T_\nu$, dominating the restoring mechanism and balancing the destabilizing back-pressure Δp acting to bring the magnet in contact with the wall, stalling the pump under Coulombic friction. For more details, see *SI Appendix*, section A.5.

Next, we address the force-balance equations governing our system's nonlinear dynamics in leading order. The magnet force-balance equations detail the dynamic balance of Maxwell stress terms, as are the result of dipole–dipole interaction between magnet and solenoid, with those from viscosity, gravity, and the rheology, with the latter resulting from the ferrofluid held by the magnetic field of the permanent magnet,

$$\hat{Z}: \underbrace{f_{b,2\to1,z}^{(0)}}_{\substack{\text{Magnetic dipole}\\\text{Maxwell force}}} + \underbrace{\int_0^{2\pi}\int_{-l/2}^{l/2}\mu\left(\frac{\partial u_z^{(0)}}{\partial\tilde{r}}\right)\bigg|_{\tilde{r}=0} dz\, l\varepsilon d\theta}_{\text{Circumferential friction pressure drop}}$$

$$- \underbrace{ma_z}_{\substack{\text{External system}\\\text{acceleration}\\\text{force, } z-axis}} - \underbrace{\pi(l\varepsilon)^2\Delta p}_{\substack{\text{Pressure drop}\\\text{across piston}}} = 0, \qquad \textbf{[1.4]}$$

$$\hat{\tilde{r}}: \underbrace{f_{b,2\to1,\tilde{r}}^{(0)}}_{\substack{\text{Magnetic dipole}\\\text{Maxwell force}}} + \underbrace{\left(\int_0^{2\pi}\int_{-l/2}^{l/2} - p^{(0)}\cos(\theta)dz\, l\varepsilon d\theta\right)\cos(\beta)}_{\substack{\text{Axial viscous pressure lift}\\\text{force}}}$$

$$+ \underbrace{\kappa_f l\varepsilon\lambda(t)}_{\substack{\text{Ferrofluid}\\\text{elastic}\\\text{force}}} - \underbrace{ma_{\tilde{r}}}_{\substack{\text{External system}\\\text{acceleration}\\\text{force, } \tilde{r}-axis}} + \underbrace{\gamma\mu u_m C}_{\substack{\text{Center} - of\\-pressure\\\text{force}}} = 0, \qquad \textbf{[1.5]}$$

where μ and κ_f are the ferrofluid's effective dynamic viscosity and linear spring coefficient, and γ is the center-of-pressure coefficient that relates the forward velocity to the destabilizing normal force in the $\tilde{r}$ direction exerted on the levitated magnetic piston, which acts as an inverted pendulum.
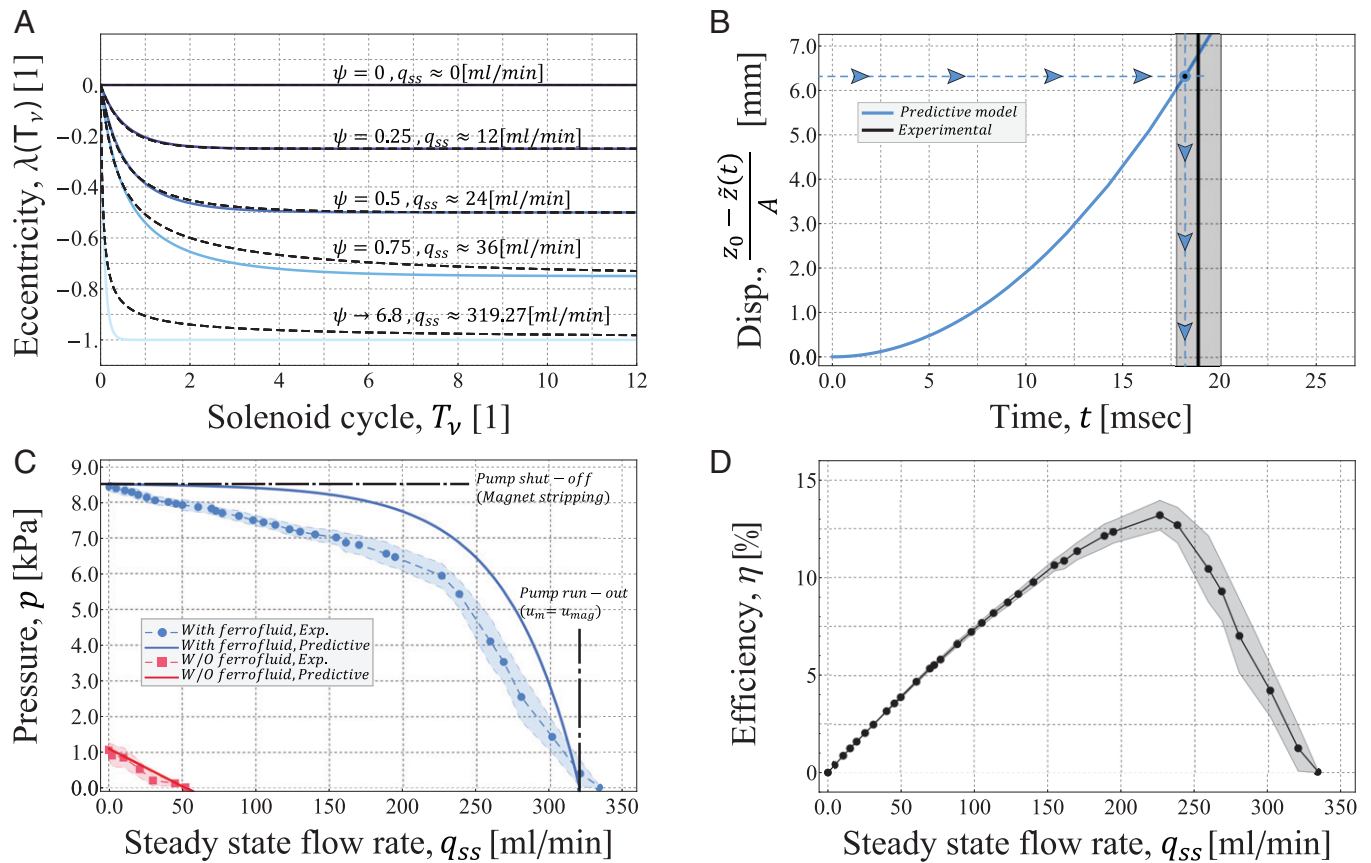
Fig. 4. Numerical, experimental, and theoretical results of magnet dynamics and pump-performance curve. (*A*) The time evolution of magnet eccentricity from an initial concentric position (at $\lambda = 0$) for different values of $\psi = \gamma \mu u_m / \kappa_f = \gamma \mu z_0 / \kappa_f \tau_r$, by varying the relay time period τ_r. Presented is a quantitative comparison between the numerical solution (dashed black lines) of the exact expression [**1.8**] and its explicit leading-order asymptotic approximation [**1.9**] in solid lines. (*B*) Comparison of theoretical (pale blue) and experimental (black) minimal relay time $\tau_{r,min}$. In pale blue is the solution to Eq. **1.10** under specified conditions for minimal relay time. The horizontal dashed line represents the distance between one solenoid to the next $(z_0 - \tilde{z}(t))/A = 6.315$ mm; the intersecting vertical dashed line informs magnet's minimal travel time. The solid black line indicates the experimental approximation of relay time based on pump run-out, $\tau_{r,min,exp} = 0.0188 \pm 0.0007$ s; error is determined based on flow-sensor specifications. (*C*) Comparison of theoretical (solid lines) and experimental pump-performance curves at unstrained state, with (dashed pale blue) and without (dashed red) the ferrofluid coating. Marked thresholds indicate pump run-out and shut-off. (*D*) Experimental characterization of pump efficiency defined $\eta = (fluid \ power)/(Solenoid \ input \ power) = pq_{ss}/V_s I$, with peak efficiency of $\eta \approx 12.5\%$ reached at $q_{ss} \approx 225$ mL·min^{-1} (corresponding to a back-pressure $\Delta p \approx 6$ kPa when intersected with *C*). Error bands for *C* and *D* indicate a 68% confidence (one SD) in the mean based on seven experiments over five separate pumps. Disp., displacement.

For simplicity, we formulate $f_{b,2\rightarrow1}$, the force applied by the solenoid (marked by index 2) on the permanent magnet (marked by index 1), using Ampere's model (66–73) to formulate the magnet–solenoid interaction. We assume the leading-order contribution is attributed to a point-like dipole–dipole interaction, with negligible correction resulting from mutual induction and magnet geometry (*SI Appendix*, section A.5.2). We then formulate the magnetic dipole Maxwell force,

$$\underbrace{f_{b,2\rightarrow1}}_{\substack{\text{Force by the magnetic} \\ \text{field of 2 acting on 1}}} = -\underbrace{\frac{3\mu_0\mu_r m_{1,z} N l_c I \pi r_{ow}^2}{4\pi\left(\sqrt{C^2\lambda^2 + \tilde{z}(t)^2}\right)^4}}_{\text{Force scalar magnitude}}$$

$$\left(\underbrace{\frac{C^3\lambda^3 - 4C\lambda\,\tilde{z}(t)^2}{\left(\sqrt{C^2\lambda^2 + \tilde{z}(t)^2}\right)^3}}_{\hat{r}}, \underbrace{0}_{\hat{\theta}}, \underbrace{\frac{3\,\tilde{z}(t)C^2\lambda^2 - 2\tilde{z}(t)^3}{\left(\sqrt{C^2\lambda^2 + \tilde{z}(t)^2}\right)^3}}_{\hat{z}} \right),$$

$$[\textbf{1.6}]$$

where $\mu_0 = 4\pi \times 10^{-7}$ N·A^{-2} is the permeability of free space; μ_r [1] the relative permeability of the ferrofluid; $m_{1,z}$ A·m^2 the permanent magnet magnetic moment; $N[winding$ m$^{-1}]$ wire-coiling density or the number of windings per unit length, assuming all are a single-layer winding; I A the current running through the coil; and l_c m the length of a single solenoid coil.

Under the above assumptions, of downstream fluid velocity u_m equals averaged magnet forward velocity u_{mag}, actuation periodicity can be related to dipole–dipole actuation distance as a function of time by the sawtooth wave function,

$$\tilde{z}(t) = u_m\tau_r\left(1 - \frac{A}{2} + \frac{A}{\pi}Arctan\left(Cot\left(\frac{\pi\,t}{\tau_r}\right)\right)\right), \quad [\textbf{1.7}]$$

where τ_r is the solenoid relay period time, which is the period for the successive coil actuation, and A [1] the temporal coordinate strain coefficient constraining an upper limit for the magnetic force during actuation in the proposed simplified model (*SI Appendix*, section A.5.2). Substituting [**1.2**], [**1.3**], [**1.6**], and [**1.7**] into our force balances Eqs. **1.4** and **1.5**, setting $\Delta p_{pump} = \Delta p$, thus requiring force equilibrium between pump and external load; last, applying scaling arguments for magnet length $Z = z/l$, gap coordinate $R = \tilde{r}/C$, time normalized by

effective downstream fluid velocity $T_\nu = t/t_\nu^* = u_m t/l$, gap height $H = h/C$, fluid field pressure $P = p/p^*$, and velocities $U_z = u_z/u_m$, $U_\theta = u_\theta/u_r^*$, and $U_r = u_r/u_r^*$, with the measure of eccentricity λ intrinsically nondimensional thus remains unchanged. We obtain a nondimensional leading-order force balance in the $\tilde{r}$ axis detailing the transient of magnet position during pumping operation,

$$\left(\frac{t^*}{t_\nu^*}\right) \underbrace{\frac{\left(2\lambda^2(T_\nu)+1\right)}{\left(1-\lambda^2(T_\nu)\right)^{5/2}}\frac{\partial\lambda(T_\nu)}{\partial T_\nu}}_{\substack{\text{Axial viscous pressure} \\ \text{force term}}} + \underbrace{\lambda(T_\nu)}_{\substack{\text{Ferrofluid} \\ \text{elastic} \\ \text{lift} \\ \text{force term}}} - \underbrace{\varrho}_{\substack{\text{System} \\ \text{acceleration} \\ \text{force term}}} + \underbrace{\psi}_{\substack{\text{Center} - of \\ -\text{pressure} \\ \text{force term}}} = 0,$$

[1.8]

with resulting characteristic scales for viscous-elastic time scale $t^* \sim \pi l\mu/\epsilon^2 \kappa_f$, the kinematic time scale $t_\nu^* \sim l/u_m$, and two non-dimensional numbers $\varrho = (radial\ acceleration)/(Elastic\ forces) = ma_{\tilde{r}}/\kappa_f C$ and $\psi = (Destabilizing\ pressure)/(Elastic\ forces) = \gamma\mu u_m/\kappa_f$. Using singular asymptotic expansion, we obtain an approximate explicit solution in leading-order (*SI Appendix*, section A.5.3),

$$\lambda(T_\nu) \approx \frac{(\varrho-\psi)\left(e^{\varrho T_\nu\left(\frac{t_\nu^*}{t^*}\right)+T_\nu\left(\frac{t_\nu^*}{t^*}\right)} - e^{T_\nu\psi\left(\frac{t_\nu^*}{t^*}\right)}\right)}{\varrho e^{T_\nu\psi\left(\frac{t_\nu^*}{t^*}\right)} + e^{\varrho T_\nu\left(\frac{t_\nu^*}{t^*}\right)+T_\nu\left(\frac{t_\nu^*}{t^*}\right)} - \psi e^{T_\nu\psi\left(\frac{t_\nu^*}{t^*}\right)}}.$$

[1.9]

Good agreement is evident in predicting the magnet position's time evolution between the numerical solution of [1.8] and the leading-order explicit approximation [1.9] (Fig. 4A).

The z axis provides us with the pressure to flow-rate relation and subsequent performance curve for ESPs,

$$\beta \underbrace{\frac{1}{\tilde{Z}^4(T_\nu)}}_{\substack{\text{Magnetic dipole} \\ \text{Maxwell force} \\ \text{term}}} - \underbrace{\frac{2}{\sqrt{1-\lambda^2(T_\nu)}}}_{\substack{\text{Viscous friction} \\ \text{pressure drop} \\ \text{term}}} - \underbrace{\zeta}_{\substack{\text{System} \\ \text{acceleration} \\ \text{force term}}} - \underbrace{2\Delta P}_{\substack{\text{Pressure drop} \\ \text{across piston} \\ \text{term}}} = 0;$$

[1.10]

along with respective nondimensional numbers $\beta = (maxwell\ force)/(viscous\ force) = 3\mu_0\mu_r m_{1,z} Nl_c I\pi r_{ow}^2 \tau_r/2\pi^2\ z_0^4\mu l$ and $\zeta = (Inertial\ force)/(viscous\ force) = ma_z/\mu u_m\pi l$.

Eqs. 1.8–1.10 give rise to three key results. The first, with viscous friction pressure drop governed by the axial position of the magnetic piston: By manipulating the viscous-elastic time scale such that $t^* \gg \tau_d = 2(n-1)\tau_r$, where n is the number of coils in the pump, we can postpone the steady-state—i.e., maximal axial displacement—for the duration of intermediate continuous operation, reducing energy losses to dissipation. Second, by limiting for $\Delta p = 0$ and $\lambda(t) \to 0$, we simulate the absence of a destabilizing force. We then substitute $u_m = \partial\tilde{z}/\partial t$, $a_z = \partial^2\tilde{z}/\partial t^2$, $\tilde{z}(t) = z_0 - A(\partial\tilde{z}/\partial t)t$, and $m = (m_m + m_w)$, where m_m is the mass of the magnet and $m_w = m_{w,pump} + m_{w,tubing}$ being the pump internal fluid mass and setup tubing fluid mass, respectively; if we then reinstitute scaling arguments and solve for τ_r, we obtain a numerical estimate for minimal relay time $\tau_{r,min}$ required to travel the distance z_0 from solenoid to solenoid (*SI Appendix*, Fig. S4B). From it, an assessment for max flow rate possible by our system $q_{max} = (z_0/\tau_{r,min})\pi(r_m + C)^2$ can then be derived. Above this limit, the magnet strips off the solenoid-train due to viscous shear stresses and inertia, inhibiting magnet acceleration. Third, and most importantly, solving [1.

10] for Δp, substituting $u_m = q/\pi r_w^2$ and [1.9], and then reinstituting scaling arguments, we obtain the pump-pressure evolution $\Delta p(t)$. Integrating over a single pumping duty cycle period τ_d and averaging over time, we obtain the pump-performance curve $\Delta p_{,DC}$,

$$\Delta p_{,DC} = -\frac{\mu l}{C^2} \underbrace{\Omega(q)}_{\text{Curve slope}}$$
$$+ \underbrace{\frac{2\pi^2\mu_0\mu_r\tau_r m_{1,z} Nl_c Ir_{ow}^2}{Al^2\tau_d z_0^4\epsilon^2}\left(\frac{1}{\left(2A\arctan\left(\cot\left(\frac{\pi\tau_d}{\tau_r}\right)\right) - \pi(A-2)\right)^3} - \frac{1}{8\pi^3}\right)}_{\text{Shut-off pressure, maximum pressure at } q=0}$$
$$- \underbrace{\frac{ma_z}{2\pi C^2}}_{\substack{\text{Acceleration} \\ \text{component}}},$$

[1.11]

with the slope $\Omega(q)$ governing the form-function of the performance. The full form of the leading-order solution is provided in *SI Appendix*, section A.5.4. However, it is of particular interest to examine the asymptotic limit when $t^*/t_\nu^* \ll 1$, for

which $\Omega(q) \sim q/\pi r_w^2 \sqrt{1 - \left(\underbrace{(a_{\tilde{r}}\ m\pi r_w^2 - \gamma C\mu q)/C\kappa_f\pi r_w^2}_{=\lambda_{ss}}\right)^2}$,

where λ_{ss} is the steady-state eccentric position of the magnetic piston, informing qualitative insights into parameters' relations to performance-curve steepness.

4.2. Pump-Performance Curve. Characterizing the performance of an existing system requires knowledge of four key parameters, μ, A, κ_f, γ. The effective linear spring coefficient κ_f and dynamic viscosity μ are material properties of the ferrofluid seal; they do not change with the system and are solely governed by the material. Opposite to them, the z-axis coordinate strain A [1] and the center-of-pressure coefficient γ [1] are two nondimensional numbers that are calculated for the specific system based on the shut-off (maximum pressure, no flow) and run-out (maximal flow, no back-pressure); these change with the system-limit values. Below, we present theoretical and experimental results for the given benchmark system. The dynamic viscosity $\mu = 0.006$ Pa·s is set constant based on the carrier fluid. The z-axis temporal coordinate strain $A \approx 0.6797[1]$ was derived from [1.11], substituting the shut-off pressure and solving for A L. The effective linear spring coefficient was experimentally evaluated to be $\kappa_f = 0.667$ N·m^{-1}, and, last, the center-of-pressure coefficient $\gamma = 2,255$ [1], as was calculated from [1.11], substituting $\Delta p_{,DC} = \Delta p = 0$, $q = q_{max}$, and solving for γ; for more details, see *SI Appendix, section A.6*.

In Fig. 4A, we plot the evolution of eccentricity $\lambda(T_\nu)$ over solenoid cycles T_ν, in units of solenoid relay time periods, as $z_0 = l$ and $u_m = u_{mag}$. Color transition from dark to light denotes an increase in ψ value and respective steady-state flow rate q_{ss} mL·min^{-1}. We show in intervals of $|\Delta\lambda_{ss}| = 0.25$ how for $\psi \ll 1$, the value ψ and $|\lambda_{ss}| = |\lambda(\infty)|$ matches, whereas transitioning from $|\lambda_{ss}| \approx 0.75$ to $|\lambda_{ss}| \to 1$ requires a disproportionate increase in ψ and, respectively, q_{ss}, an attribute of the exponential decay nature of $\lambda(T_\nu)$ as it approaches its limit at unity.

In Fig. 4B, we compare theoretical approximation to experimental results for the minimal relay time of our experimental setup. With a total accelerated mass $m = (m_m + m_w) \approx 0.009$ kg, we solve [1.10] for τ_r, as discussed in the concluding

paragraph of Section 4.1, and obtain a theoretical approximate $\tau_{r,min,Theo} = 0.0182$ s. Good agreement is seen compared with the experimental minimal relay time $\tau_{r,min,exp} = 0.0188 \pm 0.0007$ s at pump run-out; this relay time corresponds to a maximal pumping duty cycle—i.e., the frequency of the magnet to completing an entire pumping cycle $f_d = 1/\tau_d \approx 4.4 \pm 0.16$ Hz—at which the maximal flow rate of $q_{max} \approx 320$ mL/min is obtained. For more details, see *SI Appendix*, section A.6.

In Fig. 4C, we focus on the pump-performance curves at an unstrained state. We present the experimental data with (dashed pale blue) and without (dashed red) the ferrofluid coating, showcasing the fluidic seal's merit, without which the pump is rendered useless. Further, reasoning the form of the performance curve with ferrofluid, we observe how as flow rate increase from $q_{ss} \approx 50$ mL·min^{-1} (respective to $\psi \approx 1$), to $q_{ss} = q_{max} \approx 320$ mL·min^{-1} (respective to $\psi \approx 6.8$), the diminishing incremental increase in λ to unity compounded with the singularity of the curve slope $\Omega(q) \propto 1/\sqrt{1 - \lambda_{ss}^2}$ result in a nonlinear increase in curve gradient, reasoning the form of the performance curve. In addressing the particular case of pump performance without ferrofluid, we examine the asymptotic limit when $t^*/t_\nu^* \gg 1$, owing to $t^* \to \infty$ as $\kappa_f \to 0$. In this limit, the resulting performance-curve slope is $\Omega(q) \sim q\gamma/\mu\pi r_w^2$, demonstrating a constant slope governed by the center-of-pressure coefficient γ [1]. We reevaluate $\gamma = 0.2$ [1] and $A \approx 0.26$ for the no-ferrofluid case (for more details, see *SI Appendix*, section A.6) and generate the respective predictive model. Good agreement is evident between model prediction (solid lines) and experimental results (dashed lines) evaluating system-performance curves.

Last, in Fig. 4D, we experimentally evaluate pump efficiency $\eta = (fluid\ power)/(Solenoid\ input\ power) = pq_{ss}/V_sI$, where V_s V and I A are the voltage and current measured at the solenoid's inlet, respectively. We show the current system attains a peak efficiency of $\eta \approx 12.5\%$ at $q_{ss} \approx 225$ mL·min^{-1} and respective back-pressure $\Delta p \approx 6$ kPa.

Several insights and design guidelines emerge from the good agreement between experimental results and the explicit approximation of Eq. **1.11**: The characteristic scale $\beta = (maxwell\ force)/(viscous\ force) = 3\mu_0\mu_r m_{1,z} Nl_c I\pi r_{ow}^2 \tau_r / 2\pi^2 z_0^5 \mu l$ governs design-parameter requirements from the individual solenoid coils, such as $\beta \gg 1$ is a sufficient condition to ensure that the pump does not stall under the back-pressure generated by the embodied system it drives. $\zeta = (Inertial\ force)/(viscous\ force) = ma_z/\mu u_m \pi l$ and $\varrho = (radial\ accleration)/(Elastic\ forces) = ma_{\tilde{r}}/\kappa_f C$ indicate system susceptibility to external accelerations, and as long as $\zeta \ll 1$ and $\varrho \ll 1$ are maintained, any applied external accelerations to the embodied system will have no appreciable effect on pump performance. The Maxwell pressure

$$\left| (2\pi^2 \mu_0 \mu_r \tau_r m_{1,z} Nl_c Ir_{ow}^2 / Al^2 \right.$$

$$\left. \tau_d z_0^4 \varepsilon^2) \left(\left(2A\ arctan\left(cot\left(\frac{\pi\tau_d}{\tau_r} \right) \right) - \pi(A - 2) \right)^{-3} - 1/8\pi^3 \right) \right|$$

establishes a clear relation between ESP parameters informing parameters to optimize pump pressure, based upon system, material, and geometric restrictions. Finally, the asymptotic pump-performance slope $\Omega(q) \sim q/\pi r_w^2 \sqrt{1 - ((a_{\tilde{r}} m\pi r_w^2 - \gamma C\mu q)/C\kappa_f \pi r_w^2)^2}$ qualitatively indicates parameters' relation to curve steepness. To conclude, we thus offer a complete set of guidelines for the design of ESPs using goal-oriented principles.

4.3. Stable Patterns of Taylor–Saffman Instabilities under Restoring Magnetic Force.
Next, we analyze the second mechanism governing our system, correlating the above-mentioned prediction with our experiments. In our experimental system,
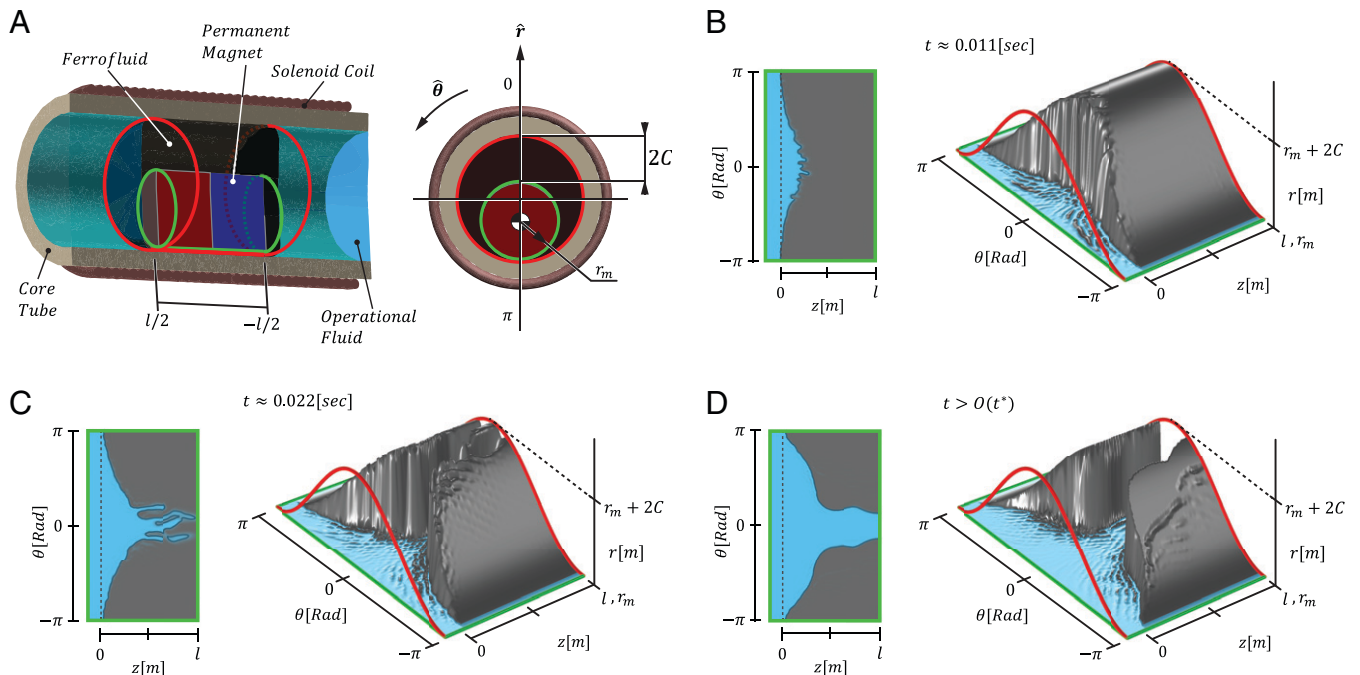

Fig. 5. Numerical simulation results for ferrofluid-seal dynamics. Presented snapshots examine ferrofluid-seal front evolution for the system at optimal duty point, $q_{ss} \approx 225$ mL·min^{-1} with respective parameters $\psi = 4.8$ and $|\lambda_{ss}| \to 1$. Ferrofluid is denoted by dark gray, pumped fluid in pale blue. (*A*) Examined configuration illustration showing dimensional notation. The inner core-tube diameter (red) and magnet outer diameter (green) are visualized to clarify the coordinate mapping in the subsequent panels. (*B*) The emergence of distinct viscous fingers (Saffman–Taylor instability) at $t \approx 0.011$ s. (*C*) Snapshot of seal front at $t \approx 0.022$ s; viscous fingers complete growth prior to seal breach. (*D*) The seal front is kept in stable oscillations past $t > O(t^*)$ s by force equilibrium between viscous and Maxwell force resultants. For the Finite Element Method (FEM) model used in plates *A*–*D*, see *SI Appendix*, section A.7.

magnet velocity $u_{mag} = z_0/\tau_r$ is held constant, dictated by the constant relay frequency $f_r = 1/\tau_r$; thus, the overall flow rate would supposedly be maintained at $q_{max} = q_{mag} = u_{mag}\pi r_w^2$. However, flow rate q mL·min^{-1} decays inversely with back-pressure Δp, as predicted by [**1.11**]. We now turn to investigate and reason the means by which a constant velocity-driven positive displacement pump provides a varying flow rate q. Utilizing the equation-based modeling capabilities of COMSOL Multiphysics 5.5, we investigate the two-dimensional (2D) flow within a Hele–Shaw cell with a variable height (for more details, see *SI Appendix,* section A.7). Based on previous work (), we investigate the emergence of Saffman–Taylor instability—i.e., viscous fingers—along the magnet length. In Fig. 5, we present a system illustration examining the transient evolution of the ferrofluid seal front from both a 2D top view and 3D projection. Snapshots show the system at optimal duty point at $q_{ss} \approx 225$ mL·min^{-1} respective to $\psi = 4.8$ and $|\lambda_{ss}| \to 1$; ferrofluid is denoted in dark gray, pumped fluid in pale blue. In Fig. 5*B*, we show the emergence of distinct viscous finger structures, the Saffman–Taylor instability; in Fig. 5*C*, viscous fingers complete growth prior to seal breach. Last, in Fig. 5*D*, we show a stable oscillating viscous finger pattern, starting at $t > O(t^*)$ s. The pattern oscillates respective to solenoid-train actuation frequency and is maintained over time by force equilibrium between viscous and Maxwell force resultant.

Through this approximate constant cross-section breach in ferrofluid seal—pale blue extension reaching from $z = 0$ to $z = l$—the ESP can maintain continuous operation under varying back-pressure without stalling.

5. Results

We now turn to demonstrate how the above model predictions and insights emerge in an experimental setup. In Fig. 6, we show the performance curve for an ESP system (constructed within the limitations of our manufacturing capabilities) evolving as we progress strain conditions. In Fig. 6 *A* and *B*, we present the steady-state performance curves under strained conditions for bending and stretching, respectively (*SI Appendix,* section A.3). It is of particular interest to examine the geometric-mechanical jamming for pump-bending deformation. We develop a simplified geometric model to determine the bounding limit for the pump-bending strain in relation to geometric parameters or vice versa. Based on our experimental system design, we estimate that mechanical jamming will occur at a bending angle $\phi_{max} \le 2\arctan(2C_e/(l/2) \approx 21.5°$, where C_e is the effective magnet gap at concentric position accounting for magnet rounded corners; for more details, see *SI Appendix,* section A.3. We did not find an equivalent mechanical jamming model for tensile strain since failure modes beyond 30% resulted from delamination at the seams, resulting from manufacturing inconsistencies. In Fig. 6*A*, we see that as the pump reaches a bending angle $\phi = 20°$, its performance approaches the point where the run-out and shut-off points intersect where it would seize.

In Fig. 7, we present a conceptual vision for functionality. Our design implements an ESP as an apparatus incorporated into a same-scale compliant boat that is forced through an obstruction course that includes 15% lateral contraction and 20° bends. The boat then emerges at the other end of the course and propels itself forward via the jet generated by the ESP (similarly to the free jet visualized in Fig. 2*F*).

We quantify the nondimensional strain rate to be $\dot{E} = (\Delta \updownarrow/\updownarrow_0)/(\Delta t/t^*) = O(10^{-2})[1]$ and normalize based on the viscous elastic time scale. We thus relate the strain rate to the governing mechanisms discussed above and in Section 4, allowing us to expand the conclusions regarding performance, mechanical jamming, and hysteresis beyond the proposed scale of this study. Data used to evaluate strain rate $\dot{E}$ are is available in *SI Appendix,* section A.8, Table S3.

Initially, we push the embodiment through the obstruction course using the semirigid outlet tube as a flexible pushrod with both inlet and outlet tubes connected. During deployment stages Fig. 7*B*, (*I*) →(*IV*), we continuously log both pressure and flow rate. In Fig. 7*A*, we illustrate the experimental setup; *Inset* illustrates a focused top view of the embodiment structure with top-level components. Fig. 7*B* shows the deployment stage (*Left*): (*I*) starting point at rest, (*II*) squeezing through a 15% lateral contraction, (*III*) 20° positive bend, and (*IV*) 20° negative bend. During (*II*) → (*III*), (*III*) → (*IV*), and past (*IV*), the system reverts to an unstrained state. Next, we present the start and end positions of the self-propulsion stage (Fig. 7 *B*, *Right*), where the system completes a swimming task, using a free jet for propulsion (as visualized in Fig. 2*G* and Movie S1). In Fig. 7*C*, we present the real-time performance of the ESP during dynamic deformation. The nonhysteretic nature of the ESP is evident upon returning to the unstrained state in sections (*II*) → (*III*) and past (*IV*); the pressure difference past section (*IV*) corresponds to change in elevation $\Delta p = \rho g h =$
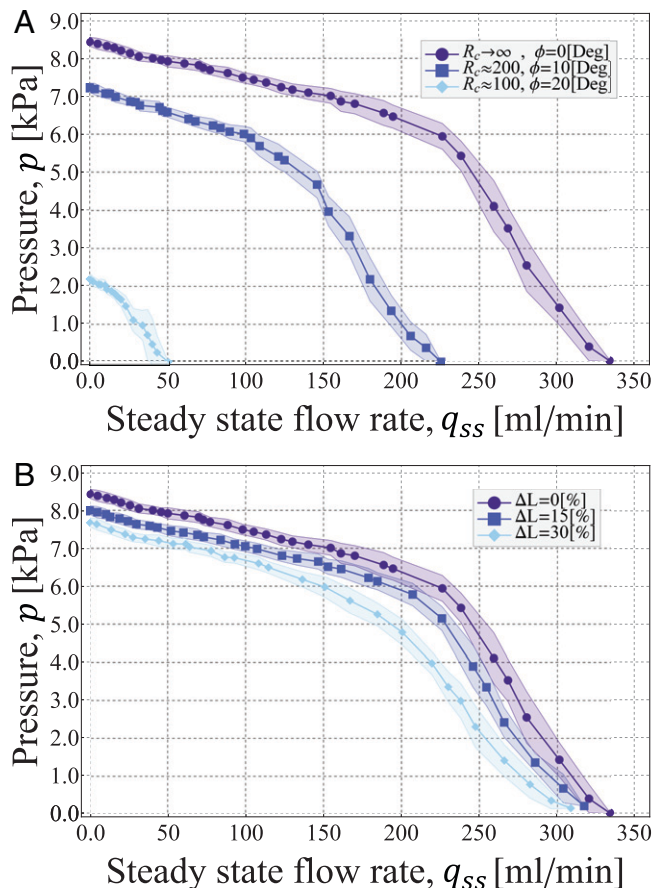
Fig. 6. Experimental performance curves of ESP under varying strain conditions. Error bands indicate a 68% confidence (one SD) in the mean based on seven experiments over five separate pumps; plot markers represent the experimental mean value. (*A*) Experimental pump performance curve at unstrained $\phi = 0°$ and strained states $\phi = 10°, 20°$. (*B*) Experimental pump performance curve at free state $\Delta L = \Delta\updownarrow/\updownarrow_0 = 0 = 0[\%]$ and axially stretched $\Delta L = \Delta\updownarrow/\updownarrow_0 = 0.15, 0.3 = 15, 30[\%]$.
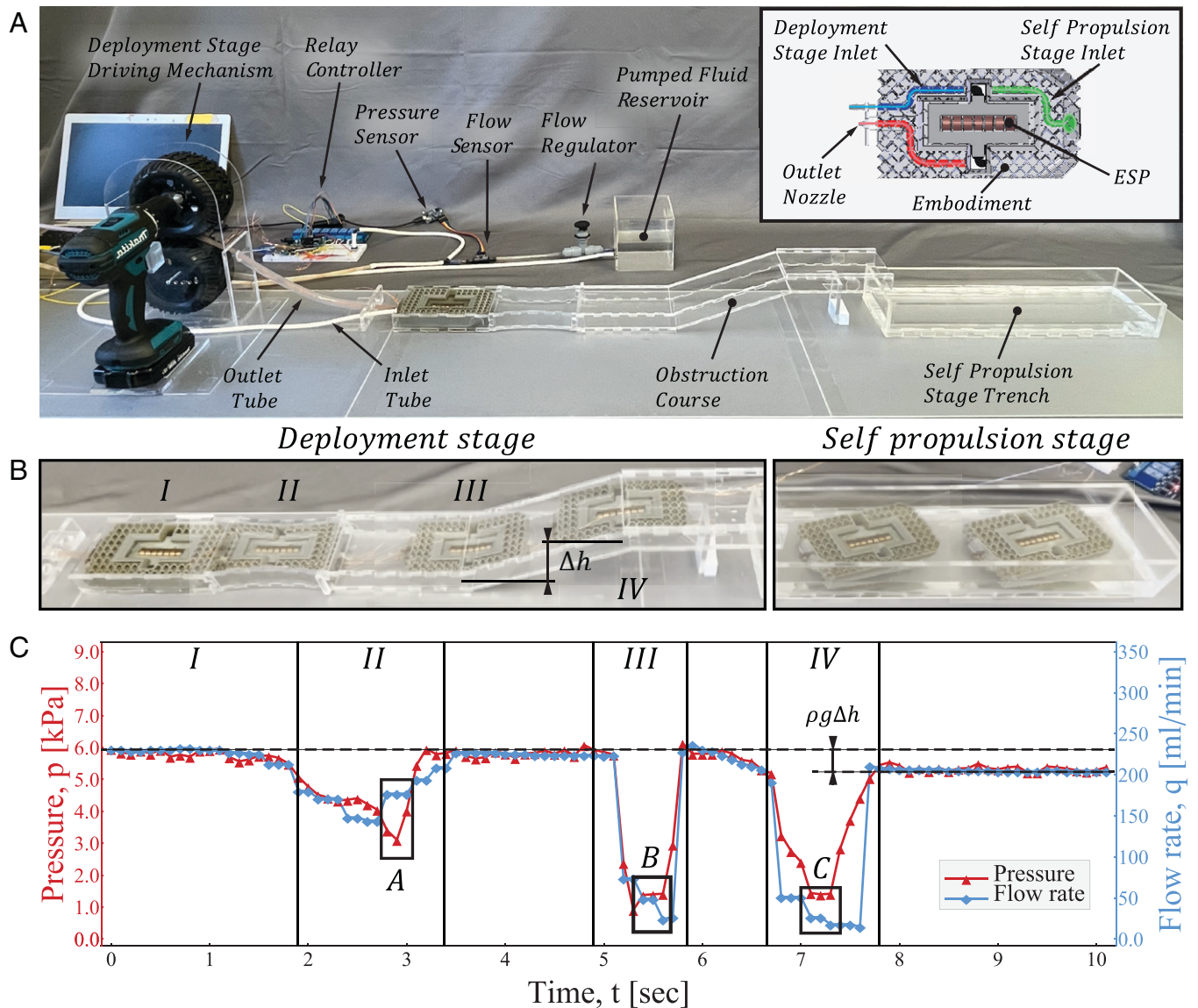
Fig. 7. Experimental setup demonstrating an ESP integrally embodied in a soft robotic apparatus. The embedded ESP endures axial and angular strain, while providing continuous fluid pressure and flow before eventually emerging at the far end. It then completes a swimming task using free jet propulsion (see jet visualization, Movie S1). (*A*) Experimental setup. *A*, *Inset* illustrates a focused top view of the embodiment structure with key top-level components. (*B*, *Left*) Deployment stage: snapshot sequence of embodiment at various stages during deployment: (*I*) starting point at rest, (*II*) lateral deformation squeezing through a 15% contraction, (*III*) 20° positive bend, and (*IV*) 20° negative bend; during (*II*)→(*III*), (*III*)→(*IV*), and past (*IV*), the system reverts to an unstrained state. (*B*, *Right*) Self-propulsion stage: start and end positions of self-propulsion postdeployment. (*C*) Continuous dynamic performance plotted in real time during deformation with evaluated nondimensional strain rate $\dot{E} = (\Delta\updownarrow/\updownarrow_0)/(\Delta t/t^*) = O(10^{-2})$[1]. Boxed regions B, and C are regions of interest, where we use the ESP for self-sensing to estimate its strained state $\varphi = \phi_{eqv}/\phi_{max} \leq 1$, thus providing a warning method prior to mechanical jamming, which occurs at $\varphi = 1$. Boxed region A ($q \approx 180$ mL·min^{-1}, $p \approx 3.1$ kPa) has an equivalent strain of $\varphi = 0.46$, whereas regions B ($q \approx 40$ mL·min^{-1}, $p \approx 1.4$ kPa) and C ($q \approx 23$ mL·min^{-1}, $p \approx 1.4$ kPa) correspond to a strained state of $\varphi = 0.93$.

$1{,}000 \times 9.81 \times 0.10 \approx 1$ kPa. A real-time video of the system navigating the course is available (Movies S5 and S6).

Last, we offer an avenue for using the ESP apparatus as a self-sensor to estimate its strained state, defined as $\varphi = \phi_{eqv}/\phi_{max} \leq 1$, and provide a warning mechanism prior to mechanical jamming. Correcting for back-pressure from the external load, we can plot the dynamic duty point—i.e., pressure and flow rate at a point in time—and overlay on Fig. 6*A*; we can then estimate the equivalent bending ϕ_{eqv} and calculate the strained state ratio φ, where $\varphi = 1$ indicates the system jamming limit. In Fig. 7*C*, boxed region A ($q \approx 180$ mL·min^{-1}, $p \approx 3.1$ kPa) has an equivalent strain $\phi_{eqv} = 10°$ respective to a strained state of $\varphi = 0.46$, whereas regions B ($q \approx 40$ mL·min^{-1}, $p \approx 1.4$ kPa) and C ($q \approx 23$ mL·min^{-1}, $p \approx 1.4$ kPa) correspond with the equivalent strain $\phi_{eqv} = 20°$ for a strained state of $\varphi = 0.93$, informing proximity to pump stalling.

6. Concluding Remarks

In this work, we tackle the leading component standing in the way of soft robotic systems from functioning under deformation—the pump. We present a simple, focused experimental demonstration and a theoretical framework, showing an ESP undergoing deformations of its own length scale $O(10^{-2})$ m, while generating pressures and flow rates in the order of $O(10^5)$ Pa and $O(10^2)$ mL·min^{-1} for a power consumption of $O(10^{-1})$ W. The resulting work-point is the largest reported for pumps that operate under large deformations (of its own length scale) with no appreciable hysteresis.

We observe two governing physical mechanisms in these systems: magnetohydrodynamic levitation and the Saffman–Taylor instability in the presence of a restoring magnetic force. In addition,

we report the characteristic scales and an explicit leading-order predictive model detailing how the proposed governing mechanism of magnetohydrodynamic lubrication is scalable with respect to pressure, flow rate, size, and radius of curvature.

Last, we elucidate a list of avenues for tailoring performance in goal-oriented design: We show how the restoring force centering the magnetic piston and the maximal pressure generated by the pump are inversely proportional to the magnet–wall gap squared, evident by the characteristic pressure scale $p^* \propto 1/C^2$. We relate ferrofluid's effective dynamic viscosity μ and linear spring coefficient κ_f to the destabilizing force acting on the magnetic piston, whereby in making $\psi \propto \mu/\kappa_f \ll 1$, we reduce steady-state eccentricity $|\lambda_{ss}|$ and, therefore, viscous friction—a leading-order source of dissipative energy loss. We point to a criterion over the nondimensional numbers ζ and ϱ, the inertial to viscous force ratios, such that when $\zeta \ll 1$ and $\varrho \ll 1$, external accelerations exerted on the pump will have no appreciable effect on performance. We provide minimal criteria sufficient to ensure that the pump does not stall under the back-pressure, so long that the nondimensional number β, the Maxwell to viscous force ratio, $\beta \gg 1$. We show the ESP apparatus as a sensor to estimate its own strained state, defined $\varphi = \phi_{eqv}/\phi_{max} \leq 1$, and provide a warning mechanism prior to mechanical jamming due to excessive deformation. Last, we inform how by manipulating the viscous-elastic time scale to be greater than the pumping duty cycle $t^* \gg \tau_d$, we can delay the magnetic piston from stabilizing at steady-state maximal eccentricity during operation, further reducing energy loss and dissipation.

Combined, these provide an explicit set of scaling laws—a toolbox to assist in goal-oriented design, a first step toward developing a practical deformable pump that will serve as the foundation for future advances in soft-pump technology.

1. K. Suzumori, S. Iikura, H. Tanaka, Development of flexible microactuator and its applications to robotic mechanisms. *Proc. IEEE Int. Conf. Robot. Autom.* **2**, 1622–1627 (1991).
2. K. Suzumori, A. Koga, F. Kondo, R. Haneda, Integrated flexible microactuator systems. *Robotica* **14**, 493–498 (1996).
3. B. Tondu, P. Lopez, Modeling and control of McKibben artificial muscle robot actuators. *IEEE Contr. Syst. Mag.* **20**, 15–38 (2000).
4. K. Suzumori, S. Endo, T. Kanda, N. Kato, H. Suzuki, "A bending pneumatic rubber actuator realizing soft-bodied manta swimming robot" in *Proceedings 2007 IEEE International Conference on Robotics and Automation* (IEEE, Piscataway, NJ, 2007), pp. 4975–4980.
5. R. F. Shepherd et al., Multigait soft robot. *Proc. Natl. Acad. Sci. U.S.A.* **108**, 20400–20403 (2011).
6. F. Ilievski, A. D. Mazzeo, R. F. Shepherd, X. Chen, G. M. Whitesides, Soft robotics for chemists. *Angew. Chem. Int. Ed. Engl.* **50**, 1890–1895 (2011).
7. R. F. Shepherd, A. A. Stokes, R. M. D. Nunes, G. M. Whitesides, Soft machines that are resistant to puncture and that self seal. *Adv. Mater.* **25**, 6709–6713 (2013).
8. R. Deimel, O. Brock, "A compliant hand based on a novel pneumatic actuator" in *2013 IEEE International Conference on Robotics and Automation* (IEEE, Piscataway, NJ, 2013), pp. 2047–2053.
9. M. A. Meller, M. Bryant, E. Garcia, Reconsidering the McKibben muscle: Energetics, operating fluid, and bladder material. *J. Intell. Mater. Syst. Struct.* **25**, 2276–2293 (2014).
10. M. T. Tolley et al., A resilient, untethered soft robot. *Soft Robot.* **1**, 213–223 (2014).
11. B. Mosadegh et al., Pneumatic networks for soft robotics that actuate rapidly. *Adv. Funct. Mater.* **24**, 2163–2170 (2014).
12. B. N. Peele, T. J. Wallin, H. Zhao, R. F. Shepherd, 3D printing antagonistic systems of artificial muscle using projection stereolithography. *Bioinspir. Biomim.* **10**, 055003 (2015).
13. B. C. Mac Murray et al., Poroelastic foams for simple fabrication of complex soft robots. *Adv. Mater.* **27**, 6334–6340 (2015).
14. A. Argiolas et al., Sculpting soft machines. *Soft Robot.* **3**, 101–108 (2016).
15. A. Zatopa, S. Walker, Y. Menguc, Fully soft 3D-printed electroactive fluidic valve for soft hydraulic robots. *Soft Robot.* **5**, 258–271 (2018).
16. D. Drotman, S. Jadhav, D. Sharp, C. Chan, M. T. Tolley, Electronics-free pneumatic circuits for controlling soft-legged robots. *Sci. Robot.* **6**, eaay2627 (2021).
17. A. Nagarkar et al., Elastic-instability-enabled locomotion. *Proc. Natl. Acad. Sci. U.S.A.* **118**, e2013801118 (2021).
18. C. A. Aubin et al., Electrolytic vascular systems for energy-dense robots. *Nature* **571**, 51–57 (2019).
19. V. Cacucciolo et al., Stretchable pumps for soft machines. *Nature* **572**, 516–519 (2019).
20. R. S. Diteesawat, T. Helps, M. Taghavi, J. Rossiter, Electro-pneumatic pumps for soft robotics. *Sci. Robot.* **6**, eabc3721 (2021).
21. C. Cao, X. Gao, A. T. Conn, A magnetically coupled dielectric elastomer pump for soft robotics. *Adv. Mater. Technol.* **4**, 1900128 (2019).
22. C. Stergiopulos et al., "A soft combustion-driven pump for soft robots" in *Proceedings of the ASME 2014 Conference on Smart Materials, Adaptive Structures and Intelligent Systems* (American Society of Mechanical Engineers, New York, 2014), vol. 2, V002T04A011.
23. W. Tang et al., Customizing a self-healing soft pump for robot. *Nat. Commun.* **12**, 2247 (2021).
24. A. Jahanshahi, F. Axisa, J. Vanfleteren, Fabrication of a biocompatible flexible electroosmosis micropump. *Microfluid. Nanofluidics* **12**, 771–777 (2012).
25. P. Kawun, S. Leahy, Y. Lai, A thin PDMS nozzle/diffuser micropump for biomedical applications. *Sens. Actuators A Phys.* **249**, 149–154 (2016).
26. Y. Tanaka, Y. Noguchi, Y. Yalikun, N. Kamamichi, Earthworm muscle driven bio-micropump. *Sens. Actuators B Chem.* **242**, 1186–1192 (2017).
27. M. Wehner et al., An integrated design and fabrication strategy for entirely soft, autonomous robots. *Nature* **536**, 451–455 (2016).
28. C. D. Onal, X. Chen, G. M. Whitesides, D. Rus, "Soft mobile robots with on-board chemical pressure generation" in *Robotics Research*, H. I. Christensen, O. Khatib, Eds. (Springer Tracts in Advanced Robotics, Springer International Publishing, Cham, Switzerland, 2017), **vol. 100**, pp. 525–540.
29. A. Olsson, P. Enoksson, G. Stemme, E. Stemme, Micromachined flat-walled valveless diffuser pumps. *J. Microelectromech. Syst.* **6**, 161–166 (1997).
30. L.-S. Jang et al., A stand-alone peristaltic micropump based on piezoelectric actuation. *Biomed. Microdevices* **9**, 185–194 (2007).
31. K. F. Lei et al., A vortex pump-based optically-transparent microfluidic platform for biotech and medical applications. *Proc. Inst. Mech. Eng. H* **221**, 129–141 (2007).
32. A. Richter, A. Plettner, K. A. Hofmann, H. Sandmaier, A micromachined electrohydrodynamic (EHD) pump. *Sens. Actuators A Phys.* **29**, 159–168 (1991).
33. S.-H. Ahn, Y.-K. Kim, Fabrication and experiment of a planar micro ion drag pump. *Sens. Actuators A Phys.* **70**, 1–5 (1998).
34. C.-H. Chen, J. G. Santiago, A planar electroosmotic micropump. *J. Microelectromech. Syst.* **11**, 672–683 (2002).
35. R. Zengerle, J. Ulrich, S. Kluge, M. Richter, A. Richter, A bidirectional silicon micropump. *Sens. Actuators A Phys.* **50**, 81–86 (1995).
36. A. Homsy, V. Linder, F. Lucklum, N. F. de Rooij, Magnetohydrodynamic pumping in nuclear magnetic resonance environments. *Sens. Actuators B Chem.* **123**, 636–646 (2007).
37. M. Ashouri, M. B. Shafii, A. Moosavi, Theoretical and experimental studies of a magnetically actuated valveless micropump. *J. Micromech. Microeng.* **27**, 015016 (2016).
38. F. C. M. Van de Pol, H. T. G. Van Lintel, M. Elwenspoek, J. H. J. Fluitman, A thermopneumatic micropump based on micro-engineering techniques. *Sens. Actuators A Phys.* **21**, 198–202 (1990).
39. W. Y. Sim, H. J. Yoon, O. C. Jeong, S. S. Yang, A phase-change type micropump with aluminum flap valves. *J. Micromech. Microeng.* **13**, 286–294 (2003).
40. J.-Y. Jung, H.-Y. Kwak, Fabrication and testing of bubble powered micropumps using embedded microheater. *Microfluid. Nanofluidics* **3**, 161–169 (2007).
41. S. A. M. Shaegh et al., Plug-and-play microvalve and micropump for rapid integration with microfluidic chips. *Microfluid. Nanofluidics* **19**, 557–564 (2015).
42. M. Zhou et al., Miniaturized soft centrifugal pumps with magnetic levitation for fluid handling. *Sci. Adv.* **7**, eabi7203 (2021).
43. H. S. Chang, C. Q. Chi, P. Z. Zhao, A theoretical and experimental study of ferrofluid lubricated four-pocket journal bearings. *J. Magn. Magn. Mater.* **65**, 372–374 (1987).
44. T. A. Osman, G. S. Nada, Z. S. Safar, Static and dynamic characteristics of magnetized journal bearings lubricated with ferrofluid. *Tribol. Int.* **34**, 369–380 (2001).
45. T. A. Osman, G. S. Nada, Z. S. Safar, Different magnetic models in the design of hydrodynamic journal bearings lubricated with non-Newtonian ferrofluid. *Tribol. Lett.* **14**, 211–223 (2003).
46. H. Montazeri, Numerical analysis of hydrodynamic journal bearings lubricated with ferrofluid. Engineering Tribology. Proc. IMechE. (2007).
47. P. Kuzhir, Free boundary of lubricant film in ferrofluid journal bearings. *Tribol. Int.* **41**, 256–268 (2008).
48. K. van der Wal, R. A. J. van Ostayen, S. G. E. Lampaert, Ferrofluid rotary seal with replenishment system for sealing liquids. *Tribol. Int.* **150**, 106372 (2020).
49. R. Moskowitz, Technology ferrofluids: Liquid magnetics: A space-age research spin-off finds its way out of the laboratory and into a host of lubricating and damping applications. *IEEE Spectr.* **12**, 53–57 (1975).
50. D. Kumar, P. Sinha, P. Chandra, Ferrofluid squeeze film for spherical and conical bearings. *Int. J. Eng. Sci.* **30**, 645–656 (1992).
51. S. G. E. Lampaert, Planar ferrofluid bearings: Modelling and design principles (2015). https://repository.tudelft.nl/islandora/object/uuid:e600236f-fd42-4738-bee0-9ca3b12b456f.
52. S. Lampaert, J. Spronck, R. van Ostayen, Load and stiffness of a planar ferrofluid pocket bearing. *Proc. Inst. Mech. Eng., Part J. Eng. Tribol.* **232**, 14–25 (2018).
53. A. S. T. Boots, L. E. Krijgsman, B. J. M. de Ruiter, S. G. E. Lampaert, J. W. Spronck, Increasing the load capacity of planar ferrofluid bearings by the addition of ferromagnetic material. *Tribol. Int.* **129**, 46–54 (2019).
54. G. S. Park, S. H. Park, Design of magnetic fluid linear pump. *IEEE Trans. Magn.* **35**, 4058–4060 (1999).

55. A. Hatch, A. E. Kamholz, G. Holman, P. Yager, K. F. Bohringer, A ferrofluidic magnetic micropump. *J. Microelectromech. Syst.* **10**, 215–221 (2001).

56. H. Hartshorne, C. J. Backhouse, W. E. Lee, Ferrofluid-based microchip pump and valve. *Sens. Actuators B Chem.* **99**, 592–600 (2004).

57. C. Yamahata, M. A. M. Gijs, "Plastic micropumps using ferrofluid and magnetic membrane actuation" in *17th IEEE International Conference on Micro Electro Mechanical Systems. Maastricht MEMS 2004 Technical Digest* (IEEE, Piscataway, NJ, 2004), pp. 458–461.

58. E. Kurtoğlu *et al.*, Ferrofluid actuation with varying magnetic fields for micropumping applications. *Microfluid. Nanofluidics* **13**, 683–694 (2012).

59. T. Michelson, J. Rudnick, J. Baxter, R. Rashidi, "A novel ferrofluid-based valve-less pump" in Proceedings of the ASME 2019 International Mechanical Engineering Congress and Exposition. Volume 7: 59445.*Fluids Engineering* (American Society of Mechanical Engineers, New York, 2019), vol. 7.

60. S. G. E. Lampaert, B. J. Fellinger, J. W. Spronck, R. A. J. van Ostayen, In-plane friction behaviour of a ferrofluid bearing. *Precis. Eng.* **54**, 163–170 (2018).

61. M. Paggi, A. Amicarelli, P. Lenarda, SPH modelling of hydrodynamic lubrication along rough surfaces. *Lubricants* **7**, 103 (2019).

62. D. Sfyris, A. Chasalevris, An exact analytical solution of the Reynolds equation for the finite journal bearing lubrication. *Tribol. Int.* **55**, 46–58 (2012).

63. L. G. Leal, *Advanced Transport Phenomena: Fluid Mechanics and Convective Transport Processes* (Cambridge University Press, Cambridge, UK, 2007).

64. K. E. Beschorner, C. F. Higgs, M. R. Lovell, "Derivation of Reynolds equation in cylindrical coordinates applicable to pin-on-disk and CMP" in *STLE/ASME 2008 International Joint Tribology Conference* (American Society of Mechanical Engineers, New York, 2009), pp. 399–401.

65. X. Chen, F. Li, G. Haidak, D. Wang, S. Li, Characterizations of the oil film considering the elastohydrodynamic lubrication effect of the piston–cylinder interface. *AIP Adv.* **10**, 095017 (2020).

66. D. Hedman, M. Fjellström, Modeling the interactions between magnetic particles (2013).

67. I. S. Grant, W. R. Phillips, *Electromagnetism* (John Wiley & Sons, Hoboken, NJ, 2013).

68. D. J. Griffiths,*Introduction to Electrodynamics. (2005): 574-574.*

69. P. Campbell, *Permanent Magnet Materials and Their Application* (Cambridge University Press, Cambridge, UK, 1996).

70. P. B. Landecker, D. D. Villani, An analytic solution for the torque between two magnetic dipoles. Magnetic and Electrical Separation 10 (1970).

71. R. Ravaud, G. Lemarquand, S. Babic, V. Lemarquand, C. Akyel, Cylindrical magnets and coils: Fields, forces, and inductances. *IEEE Trans. Magn.* **46**, 3585–3590 (2010).

72. W. Robertson, B. Cazzolato, A. Zander, Axial force between a thick coil and a cylindrical permanent magnet: Optimizing the geometry of an electromagnetic actuator. *IEEE Trans. Magn.* **48**, 2479–2487 (2012).

73. J. G. Ku, X. Y. Liu, H. H. Chen, R. D. Deng, Q. X. Yan, Interaction between two magnetic dipoles in a uniform magnetic field. *AIP Adv.* **6**, 025004 (2016).

74. A. L. G. A. Coutinho, J. L. D. Alves, Finite element simulation of nonlinear viscous fingering in miscible displacements with anisotropic dispersion and nonmonotonic viscosity profiles. *Comput. Mech.* **23**, 108–116 (1999).

75. W. B. Zimmerman, G. M. Homsy, Nonlinear viscous fingering in miscible displacement with anisotropic dispersion. *Phys. Fluids A Fluid Dyn.* **3**, 1859–1872 (1991).

76. E. Holzbecher, Modeling of viscous fingering. 6. COMSOL conference, Milan. (2009).

77. R. N. Horne, F. Rodriguez, Dispersion in tracer flow in fractured geothermal systems. *Geophys. Res. Lett.* **10**, 289–292 (1983).

78. G. I. Taylor, Dispersion of soluble matter in solvent flowing slowly through a tube. *Proc. R. Soc. Lond. A Math. Phys. Sci.* **219**, 186–203 (1953).